1 In-situ Monitoring of the Polymerization Kinetics of Organic Pollutants during

2 Persulfate-based Advanced Oxidation Processes Using Plasmonic Colorimetry

3	Hanwei Wang, 1,2 Alexander Kvit, 3 Haoran Wei*1,2
4	1. Environmental Chemistry and Technology Program, University of Wisconsin–Madison,
5	660 N. Park St., Madison, Wisconsin 53706, USA
6	2. Department of Civil and Environmental Engineering, University of Wisconsin–Madison,
7	Madison, Wisconsin 53706, USA
8	3. Department of Materials Science and Engineering, University of Wisconsin–Madison,
9	1509 University Avenue, Madison, Wisconsin 53706, USA
10	
11	
12	* Corresponding author. E-mail: <u>haoran.wei3@wisc.edu</u> ; Telephone: +1 (608) 263-6278
13	
14	
15	
16	In preparation for Analytical Chemistry
17	
18	

ABSTRACT

19

20

21

22

23

24

25

26

27

28

29

30

31

32

33

34

35

36

39

Using sulfate radicals to initiate polymer production in persulfate-based advanced oxidation processes (AOPs) is an emerging strategy for organics removal. However, our understanding of this process remains limited due to a dearth of efficient methods for in-situ and real time monitoring of polymerization kinetics. This study leverages plasmonic colorimetry to monitor the polymerization kinetics of an array of aromatic pollutants in the presence of sulfate radicals. We observed that the formation of polymer shells on the surfaces of gold nanoparticles (AuNPs) led to an increase and red shift in their localized surface plasmon resonance (LSPR) band, as a result of an increased refractive index surrounding the AuNP surfaces. This observation aligns with Mie theory simulations and transmission electron microscopy-electron energy loss spectroscopy characterizations. Our study demonstrated that the polymerization kinetics exhibit a significant reliance on the electrophilicity and quantity of benzene rings, the concentration of aromatic pollutants, and the dosage of oxidants. In addition, we found that changes in LSPR band wavelength fitted well into a pseudo-first-order kinetics model, providing a comprehensive and quantitative insight into the polymerization kinetics involving diverse organic compounds. This technique holds the potential for optimizing AOP-based water treatment by facilitating the polymerization of aromatic pollutants.

KEYWORDS

- 37 Plasmonic colorimetry, Localized surface plasmon resonance, Persulfate-based advanced
- 38 oxidation processes, Industrial wastewater, Polymerization

INTRODUCTION

Advanced oxidation processes (AOPs) are widely adopted stratagies to alleviate the pollution of recalcitrant and non-biodegradable organic chemicals in water and wastewater treatment due to their remarkable efficiency and effectiveness. AOPs rely on *in-situ* generation of highly reactive species, such as hydroxyl and sulfate free radicals, which exhibit extensive decomposition capabilities across a broad spectrum of pollutants. Persulfate-based AOPs have recently attracted tremendous interest because of several advantages of sulfate radicals ($SO_4^{\bullet\bullet}$) over hydroxyl radicals (OH), such as higher redox potential at circumneutral pH ([$E_0(SO_4^{\bullet\bullet}/SO_4^{2-}) = 2.5-3.1 \text{ V}$ vs. $E_0(OH/OH) = 1.8 \text{ V}$), longer lifetime, and higher selectivity. Sulfate radicals can be readily generated through photo, thermal, hermal, and catalytical activitation of their precursors, such as peroxydisulfate (PDS) and peroxymonosulfate (PMS).

The ultimate goal of AOPs is to achieve complete mineralization of organic pollutants in order to effectively decontaminate water. Unfortunately, targeted pollutants and natural organic matter can be transformed into undesired and potentially more harmful byproducts during AOPs depending on water matrix compositions and peroxide dosages.^{2, 7, 9, 13} Polymers are one of the commonly formed byproducts during AOPs, as free radicals are well-known initiators for aromatic compound polymerization.¹⁴ Despite the fact that polymerization substantially diminishes the efficiency of organic pollutant mineralization, recent studies have proposed that the formation of polymers in persulfate-based AOPs can be utilized as an innovative strategy for organic pollutant abatement.^{10, 15, 16} This strategy excels due to the lower peroxide consumption required for polymerization, as well as facile separation and recovery of the resulting products from the waste stream. As an example, the polymerization-based strategy can save up to 85% of PDS in coking

wastewater treatment compared to the mineralization-based strategy, while removing the same amount of dissoved organic carbon.¹⁰

Despite the recent advances made in understanding polymerization processes during persulfate-based AOPs,¹⁷ there is still a gap in systematically investigating the polymerization kinetics of various organic pollutants under typical persulfate doses. Recent studies have generally estimated polymerization kinetics by monitoring the reduction in monomer concentrations via high-performance liquid chromatography.^{10, 15, 16, 18} The generated polymers have typically been characterized using a combination of techniques, such as scanning electron microscopy, transmission electron microscopy (TEM), electrospray ionization mass spectrometry, Fourier transform infrared spectroscopy, X-ray diffraction, and thermogravimetric analysis.^{10, 15, 16, 18} While these analytical methods provide valuable insights, they are time-consuming, expensive, and require delicate equipment along with complex sample pre-treatment procedures. More importantly, none of these techniques can provide *in-situ* and real-time acquisition of polymerization kinetics.

Plasmonic nanoparticles (PNPs) have demonstrated immense potential in sensing chemicals, biomolecules, and pathogens because of a unique optical phenomenon – localized surface plasmon resonance (LSPR).¹⁹⁻²¹ LSPR refers to the collective oscillation of conduction electrons of PNPs at a resonant frequency under the excitation of incident light,²² leading to extremely strong light extinction (i.e., absorption and scattering). The wavelength, at which LSPR occurs, is particularly sensitive to changes in the aggregation state of PNPs and the refractive index of the surrounding media,^{23, 24} both of which can be concurrently modified by the polymerization of organic pollutants in the vicinity of PNPs. Hence, monitoring the variations in LSPR through

plasmonic colorimetry can serve as a potent and untapped approach to monitoring the evolution of polymerization reaction *in situ* and in real time.

In this study, we employed plasmonic colorimetry, for the first time, to monitor the polymerization of a wide variety of organic pollutants during persulfate-based AOPs. Gold nanoparticles (AuNPs) were selected as PNP transducers due to their excellent chemical stability and biocompatibility. In the presence of SO₄-, the AuNP colloid rapidly collapsed due to the oxidation of the citrate stablizing layer on AuNP surfaces. 25 However, when aromatic compounds, such as 2,4-dichlorophenoxyacetic acid (2,4-D), bisphenol A (BPA), and diclofenac sodium (DIC), were introduced, the AuNP colloid was stablized due to the formation of polymeric layers on AuNP surfaces. TEM images confirmed polymer formation, while electron energy loss spectroscopy (EELS) characterization provided insights into the polymer compositions. We measured the polymerization kinetics of organic pollutants by monitoring the shifts of the LSPR bands, which was further corroborated by Mie theory simulations. We also explored how functional groups, halogen substitutions, and benzene ring quantities influenced the polymerization kinetics of the pollutants. This study introduces a simple and cost-effective method for quantifying the rate and extent of polymer formation during persulfate-based AOPs, aiding in the optimization of persulfate dosages and reaction times to either inhibit or promote polymerization.

EXPERIMENTAL SECTION

84

85

86

87

88

89

90

91

92

93

94

95

96

97

98

99

100

101

102

103

104

105

106

Chemicals. Chemicals used in our experiments are described in Text S1.

AuNP synthesis. AuNPs were synthesized using a seed-mediated growth method detailed in our previous study and Text S2.²⁶ The as-synthesized AuNPs were nanospheres with a uniform size distribution (43±5 nm, N=20) based on TEM analysis (Fig. S1).

In-situ monitoring of pollutant polymerization via plasmonic colorimetry. All experiments were conducted in 4-mL quartz cuvettes sealed with airtight stoppers. An aliquot of 3-mL AuNP suspension was first pipetted into a cuvette, followed by successive additions of 0.5-mL PDS solution and 0.5-mL pollutant solution. To prompt the photolysis of PDS and subsequent generation of SO₄-*, the cuvette was exposed to simulated sunlight irradiation, facillitated by a solar simulator (Abet Technologies, Milford, CT, USA). For each experiment, a parallel control was set under the same conditions in the absence of light. The extinction spectra of the described mixtures were acquired using a UV-vis spectrofluorometer (Horiba Aqualog, NJ, USA). A UV-vis spectrum was immediately recorded upon adding both PDS and pollutant stock solutions into the AuNP colloid (termed "0 min"). To monitor the kinetics of polymerization, the UV-vis spectra of the mixture were measured at 15-min intervals over a period of 2 hours after mixing. Before each spectroscopic measurement, the cuvette was gently shaken three times to ensure the thorough mixing of all internal components. More experimental details are provided in Text S3.

Characterization of the generated polymers. To confirm the generation of polymers on the AuNP surfaces, the above-mentioned mixtures after 2-hour sunlight irradiation were purified via centrifugation and resuspension. This procedure was employed to separate the AuNPs from the excess chemicals present in the suspensions. The resulting purified polymer-stabilized AuNPs were then characterized using TEM (FEI Tecnai TF30, Hillsboro, Oregon, USA) and EELS (FEI Titan 80-200, Hillsboro, Oregon, USA) to gain insights into the morphology and chemical composition of the formed polymers. Additionally, the stability of the polymer-coated AuNPs was tested under the conditions of high ionic strength. More details regarding the purification procedures, TEM and EELS characterization, as well as stability testing are described in Text S4&S5.

RESULTS AND DISCUSSION

130

131

132

133

134

135

136

137

138

139

140

141

142

143

144

145

146

147

148

149

150

151

152

In-situ Monitoring of 2,4-D polymerization kinetics via plasmonic colorimetry. Agricultural industry effluents were reported to contain a variety of aromatic pollutants with high concentrations.²⁷ 2,4-D, a widely used herbicide that is present in pesticide production wastewater,²⁷ was initially selected as a representative aromatic pollutant to test the feasibility of monitoring polymerization kinetics using plasmonic colorimetry. Upon adding 5 mM PDS and 0.23 mM 2,4-D into the AuNP colloid (labelled as "0 min" in Fig. 1a&b), the LSPR band was found at 530 nm, mirroring the pristine 43-nm AuNP colloid (Fig. S2a). Under simulated sunlight irradiation, the intensity of the LSPR band gradually increased over the first 105 min from 0.8 to 1, before stablizing in the final 15 min (Fig. 1a). Simultaneously, the wavelength of the LSPR band experienced a significant red shift from 530 to 544 nm within a 2-hour period (Fig. 1a), suggesting an increased refractive index (RI) of the medium surrounding the AuNPs. 24, 28 According to our previous study, SO₄- are readily generated by breaking the S-S bond of PDS through UV photolysis under the illumination conditions employed in this study. ²⁵ Since AuNPs exhibit weak absorption in the UV range (Fig. S2a), their influence on PDS photolysis is likely negligible. Given that SO₄-• often initiate polymerization, we expect it to aid in the formation of 2,4-D polymeric layers on the AuNP surfaces.

To verify the critical role of each component in polymer formation – namely illumination, 2,4-D, and PDS, a series of control experiments was performed. Initially, when the aforementioned experiment was conducted in the absence of light, the LSPR band intensity marginally decreased and the band wavelength remained unchanged over 2 hours (Fig. 1b). Without simulated sunlight, PDS remained predominantly as persulfate ions (S₂O₈²-), contributing less to inducing 2,4-D polymerization compared to SO₄-*. Furthermore, when the 2,4-D solution was replaced with an

equivalent volume of Milli Q water, the LSPR band significantly decreased and blue shifted during the first hour of irradiation, and disappeared completely afterwards (Fig. 1c). These results imply continuous aggregation and susequent collapse of the AuNP colloid due to the rapid oxidation of citrate stabilizing layers on AuNP surfaces.²⁵ Without simulated sunlight, the LSPR band decreased by only 25% over 2 hours, suggesting slower citrate oxidation kinetics by S₂O₈²⁻ compared to SO₄- (Fig. 1d). Additionally, when only 2,4-D was added to the AuNP colloid, there was virtually no change in the UV-vis extinction spectra over 2 hours, regardless of the presence or absence of simulated sunlight (Fig. S2b&c), demonstrating that no polymerization occurred without PDS. It is clear that for suscessful polymerization as depicted in Fig. 1a, all three components – simulated sunlight, PDS, and 2,4-D, are crucial.

Influence of PDS and 2,4-D concentrations on 2,4-D polymerization kinetics. Keeping the experimental setup consistent, we acquired the polymerization kinetics using various combinations of PDS and 2,4-D concentrations (Fig. S3). When the 2,4-D concentration was kept constant at 0.23 mM, the LSPR band wavelength consistently increased from 531 nm to 533, 537, 541, and 546 nm during 1 hour of sunlight irradiation at PDS concentrations of 1, 2.5, 5, and 10 mM, respectively (Fig. S3a). Higher PDS concentrations corresponded to larger LSPR band shift, indicating accelerated polymerization kinetics in the initial hour. In the subsequent hour, at lower PDS concentrations (i.e., 1, 2.5, and 5 mM), the LSPR bands continued to rise, accompanied by slow red shifts until reaching the plateau (Fig. 1a, S3a, S4a & S4c). Conversely, at a higher PDS concentration (i.e., 10 mM), the LSPR band started to decrease and blue shift (Fig. S3a & S4e), indicating oxidative degradation of the polymeric layers by the excess SO₄.

As the 2,4-D concentration was gradually reduced from 0.23 to 0.045 mM while the PDS concentration was maintained at 10 mM, the oxidant was more excessive, leading to an earlier blue

shift of the LSPR band (Fig. S3c). Similar to the trend observed at the higher 2,4-D concentration (0.23 mM), the LSPR band initially red shifted to 535 nm in the first 30 min, and subsequently blue shifted to 523 nm at a 2,4-D concentration of 0.11 mM (Fig. S3c & S5e). The LSPR band wavelength at the 2-hour point even fell below its initial value, indicating that the surface coatings, including the polymer and citrate, were significantly removed due to the oxidation induced by SO₄⁻¹. When the 2,4-D concentration dropped below 0.1 mM, the LSPR bands only experienced blue shifts within 45 min before disappearing entirely (Fig. S3c, S5a, & S5c), which was attributed to the rapid removal of citrate coatings on AuNP surfaces and the resulting colloid collapse.

Polymerization kinetics were found to be dependent on the concentration ratio of PDS to 2,4-D. With a ratio below 22, polymer growth persisted until all SO₄⁻⁻ were completely consumed, with the growth rate decreasing as the ratio further decreased (Fig. S3a). Conversely, at a ratio exceeding 43, polymer growth ensued until 2,4-D was fully consumed, followed by degradation or complete removal of the polymer by the excess SO₄⁻⁻ (Fig. S3c). Nevertheless, further results indicated that maintaining a consistent ratio does not necessarily lead to consistent outcomes. By preserving the PDS-to-2,4-D ratio at 22 while lowering the PDS and 2,4-D concentrations by factors of 2 and 5, respectively, significantly slower polymerization kinetics were observed (Fig. S3e and Fig. S6a&c). Therefore, both the absolute concentrations and the concentration ratios of the organic substrate (2,4-D) and the oxidant (PDS) play equally important roles in polymerization kinetics. As shown in Fig. S3b,d,&f, Fig. S4b,d,&f, Fig. S5b,d,&f, and Fig. S6b&d, the LSPR bands remained relatively consistent during 2 hours under dark conditions, irrespective of the organic substrate and oxidant concentrations. This further reinforces the instrumental role of SO₄⁻ in driving 2,4-D polymerization.

Dramatically different polymerization kinetics of aromatic and aliphatic carboxylates.

To further understand the SO₄*-induced polymerization of 2,4-D, model aromatic and aliphatic carboxylates representing different moieties of 2,4-D, including 2-CBA, 3-CBA, 4-CBA, acetic acid, and chloroacetic acid, were selected as the target analytes. When adding 5 mM PDS and 0.64 mM 2-CBA into the AuNP colloid, the LSPR band intensity gradually increased, and its wavelength shifted from 531 to 551 nm after 2 hour of simulated sunlight irradiation (Fig. S7a). These findings align closely with those from the 2,4-D tests, showcasing the rapid polymerization of 2-CBA when light, chemical substrate, and PDS were simultaneously present. The polymerization kinetics of 2-CBA were investigated across varied combinations of PDS and 2-CBA concentrations (Fig. S7, Fig. S8, Fig. S9, Text S6).

Generally, an excess of aromatic carboxylates resulted in a continuous generation of polymers, evident from the red shift of the LSPR band, until the SO₄ were entirely exhausted. On the other hand, excess PDS led to a blue shift of the LSPR band due to further oxidation of the generated polymers. Similar to 2,4-D, no polymerization evidence was observed for any combinations of PDS and 2-CBA concentrations without simulated sunlight (Fig. S7b,d,&f, S8b,d,&f, S9b,d,&f). Furthermore, the indespensible role of SO₄ in polymerization was validated by replacing 10 mM PDS with a 10 mM K₂SO₄ solution, which maintained the same ionic strength but without generating SO₄. In this situation, there were no notable differences in the UV-vis spectra of the AuNP colloid between sunlit and dark condition (Fig. S10). This suggests that no polymerization occurred in the presence of K₂SO₄, unlike the observations when PDS was present (Fig. S8e&f). Two isomers of 2-CBA, namely 3-CBA and 4-CBA, were also evaluated, which demonstrated similar trends to 2-CBA when tested at equivalent concentrations (Fig. S11).

In contrast to aromatic carboxylates, aliphatic carboxylates did not show any capacity to form polymers under comparable conditions (Fig. S12). Compared to the pristine AuNP colloid with 5 mM PDS, the addition of 0.64 mM acetic acid or chloroacetic acid led to the stabilization of the AuNP colloid under simulated sunlight irradiation (Fig. 1c, S12a&c). Nevertheless, no evidence of polymerization was observed for both aliphatic carboxylates, as suggested by the constant LSPR band intensity and wavelength over a 2-hour period (Fig. S12a&c). This was a stark contrast to 2-CBA at the same concentration (Fig. S7a).

220

221

222

223

224

225

226

227

228

229

230

231

232

233

234

235

236

237

238

239

240

241

242

In-situ monitoring of phenol polymerization. Phenols and their derivatives are prevalent in various industrial wastewater effluents, such as petrochemicals, pharmaceuticals, and refineries.²⁹ Particularly, halogenation greatly enhances the recalcitrancy and toxicity of phenols,³⁰, ³¹ which underscores the importance of effective monitoring and removal of these contaminants. Consequently, phenol and three chlorophenols are selected as target analytes to explore their polymerization kinetics in the presence of SO₄. Compared to aromatic carboxylates, phenols are more reactive with SO₄, especially under basic conditions. ^{32, 33} We thus anticipate that phenols will exhibit higher polymerization kinetics than aromatic carboxylates. Similar to aromatic carboxylates, the polymerization of phenols only took place under sunlit conditions (Fig. 2a-d & S13a-d). With the presence of 0.64 mM phenol and 5 mM PDS, the LSPR band of the AuNP colloid significantly shifted from 531 to 564 nm over 2 hours, accompanied by a two-fold increase in intensity (Fig. 2a). The most substantial change in LSPR band wavelength was observed within the first 15 min (Fig. 2a), indicating dramatically faster polymerization kinetics of phenol compared to aromatic carboxylates. On the other hand, the polymerization of 2-CP exhibited a trend similar to phenol, but with slightly slower kinetics (Fig. 2b). In a recent study, the polymerization of 1 mM phenol or 2-CP in a heat/PDS system ([PDS] = 10 mM) achieved the maximum at 35 min, whereas the polymerization processes in our system ([phenol] or [2-CP] = 0.64 mM, [PDS] = 5 mM) lasted for 2 hours.¹⁰ The slower kinetics of phenol and 2-CP polymerization in our system can be attributed to the lower concentrations of the organic substrates and oxidant, which is consistent with our earlier findings (Fig. S3a&c).

Li et al. mentioned that different oxidation mechanisms could be involved in the oxidation of aromatic compounds with strong electron-withdrawing substituents, such as -Cl and -Br. ¹⁰ In this study, an analysis of three isomers of chlorophenols at the same concentration suggested that the position of halogen substition on the benzene ring significantly affected the polymerization kinetics. During the initial 15-min polymerization of 3-CP and 4-CP, the LSPR band of the AuNP colloid immediately decreased and red shifted, accompanied by the increasing light extinction within the 600-800 nm region (Fig. 2c&d). These results indicate a concurrent process of 3-CP or 4-CP polymerization and AuNP aggregation. In the subsequent 105 min, the aggregation of AuNPs did not persist as the resulting AuNP multimers were stabilized by the gradual polymerization of 3-CP or 4-CP (Fig. 2c&d). Unlike 2-CP that rapidly polymerized during the first 15 min (Fig. 2b), the polymerization kinetics of 3-CP and 4-CP were much slower. Therefore, the polymers that were generated during the initial 15-min polymerization of 3-CP and 4-CP were insufficient to stabilize the AuNP monomers, which thus exhibited strong tendency for aggregation as the citrate stabilizing layer was oxidized and the ionic strength was high.

The faster polymerization kinetics of phenolic compounds compared to aromatic carboxylates can be attributed to the weaker electron-withdrawing effect of hydroxyl groups compared to the carboxylic groups on the benzene rings. To verify this hypothesis, the hydroxyl and carboxylic groups were replaced by a nitro group that exhibits strong electron-withdrawing effect. At the same concentration with 2-CBA and 2-CP (0.64 mM), 1-chloro-2-nitrobenzene

barely polymerized in the presence of 5 mM PDS under sunlit condition (Fig. S14). This is supported by the fact that the LSPR band slightly decreased and shifted from 531 to 533 nm over 2 hours under simulated sunlight irradiation, while the LSPR band wavelength remained constant in the absence of light (Fig. S14). Consistent with previous study, the reaction rate constant of nitrobenzene with SO₄⁻⁻ was more than 3 orders of magnitude lower than that of benzoic acid.³⁴ Due to the reduced reactivity with SO₄⁻⁻, aromatic pollutants with strong electron-withdrawing substituents could exhibit significantly slower polymerization kinetics during persulfate-based AOPs.³⁵

Polymerization kinetics of aromatic pollutants with greater complexity. To further verify the effectiveness of this innovative sensing approach in monitoring polymerization, we selected two aromatic pollutants with dual benzene rings and either hydroxyl or carboxylic group s: bisphenol (BPA) and diclofenac (DIC). BPA is extensively used in the plastics and resin manufacturing industry. Known as an endocrine disruptor, BPA has garnered widespread attention due to its reproductive and developmental toxicities, as well as its potential association with diabetes and thyroid dysfunction. ³⁶⁻³⁸ DIC, a non-steroidal anti-inflammatory drug, has been detected in aquatic environments globally and recognized as an emerging contaminant. The hazardous effects of DIC residues on mammals and ecosystems are well-documented. ³⁹⁻⁴¹ Persulfate-based AOPs have proven effective ways in removing both pollutants, ⁴²⁻⁴⁵ during which polymerization may take place.

BPA, possessing two phenolic moieties, displayed peculiarly rapid polymerization kinetics in the presence of 5 mM PDS and simulated sunlight. The LSPR band of the AuNP colloid immediately shifted to the 550-600 nm range within 15 min of simulated sunlight irradiation (Fig. 2e), indicating the rapid polymerization of BPA. Pinpointing the exact wavelength of this

transverse dipole LSPR band is challenging due to its overlap with a higher-order multipole LSPR band that emerges as a consequence of AuNP aggregation. 46 Similar to 3-CP and 4-CP (Fig. 2c&d), the polymers formed within the initial 15 min were insufficient to protect AuNP monomers from aggregating, which can be attributed to the low BPA concentration (0.055 mM). However, AuNP aggregation almost stopped after 15 min as the polymeric layer on AuNP surfaces continued to grow (Fig. 2e). In comparison with 2-CBA and 4-CBA at similar concentrations (Fig. S9a & S11e), BPA showed a considerably enhanced propensity for polymerization. This is supported by the more pronounced red-shifted LSPR band and the increased stability of the AuNP colloid (Fig. 2e). This higher polymerization potential is attributed to the two phenolic moieties in one BPA molecule.

The fast polymerization kinetics of DIC further support our hypothesis that chemicals with dual benzene rings have a higher propensity to polymerize than those with a single benzene ring. With 0.31 mM DIC and 5 mM PDS, the LSPR band of the AuNP colloid shifted from 535 to 558 nm within the initial 15 min, and further shifted to 562 nm by 120 min (Fig. 2f). Simultaneously, the intensity of the LSPR band continued to increase over the 120-min period. Compared to 2-CBA and 3-CBA that possess only one benzene ring and one carboxylic group (Fig. S9e & S11c), DIC exhibited significantly faster polymerization kinetics that can be attributed to its double benzene rings. For both compounds, in the absence of simulated sunlight, the transverse dipole LSPR bands barely shifted over 120 min, indicating that no polymerization occurred (Fig. S13e&f).

Characterization of the formed polymers. The formed polymers on AuNP surfaces significantly enhanced the stability of AuNPs in environments with high ionic strength. After 2-hour simulated sunlight irradiation, the LSPR band of the AuNP colloid in the presence of 5 mM PDS and 0.64-mM 2-CBA increased and red shifted from 532 to 554 nm (Fig. S15), indicating

polymer formation on AuNP surfaces. After reaction, the polymer-coated AuNPs were purified and resuspended in a 100-mM K₂SO₄ solution (see details in Text S4). Such high ionic strength typically causes immediate aggregation of citrate-coated AuNPs, but did not detrimentally affect the stability of the polymer-coated AuNPs even after 24 h. This stability is supported by the persistent transverse LSPR band wavelength at 554 nm during 24 h and the absence of a higher-order LSPR band in the near-infrared region (Fig. S15).

312

313

314

315

316

317

318

319

320

321

322

323

324

325

326

327

328

329

330

331

332

333

334

The characterization of polymers on AuNP surfaces generated from 2,4-D, 2-CBA, and 2-CP after 2 hour of light irradiation was conducted using TEM and EELS. It is important to note that it is extremely challenging to use TEM to measure polymer thickness after 5 and 15 minutes of light irradiation (data now shown), underscoring the effectiveness of the plasmonic colorimetric method in detecting early stages of polymer growth. In comparison with the citrate-coated AuNPs (Fig. S1), the TEM images of the polymer-coated AuNPs showed a ~43 nm gold core surrounded by an opaque polymeric layer (Fig. 3a-c). Furthermore, the results of high-angle annular dark-field scanning transmission electron microscopy (HAADF-STEM) and EELS spectrum imaging indicated that the polymer shells predominantly consisted of C, while O and Cl were preferably distributed on the surfaces of AuNPs (Fig. 3d). Oxygen on the AuNP surfaces likely originates from either the citrate trapped within the polymer or the hydroxyl groups interacting with AuNPs at the initial stages of polymerization. The presence of Cl on the AuNP surfaces may arise from either residual Cl⁻ during AuNP synthesis or Cl⁻ generated during the dechlorination process. In addition, we observed a competing behavior between O and Cl for binding sites on the AuNP surfaces.

The thickness and density and of the polymeric shells were consistent among polymercoated AuNPs derived from the same chemical. However, there were notable variations when

comparing polymers derived from different chemicals. Specifically, the average shell thicknesses for 2,4-D-, 2-CBA-, and 2-CP-derived polymers were 3, 8, and 20 nm, respectively (Fig. 3a-c). While precise measurements were challenging, the densities of these polymer shells follow the order: 2,4-D < 2-CBA < 2-CP according to visual inspection of their contrast against the background in TEM images. According to the Mie theory, the LSPR of PNPs is dependent on the identity, shape, size, and aggregation state of the nanoparticles, as well as the refractive index (RI) of the surrounding medium. 47-49 To delve deeper into the effects of shell thickness and RI (indicative of shell density) on LSPR, the extinction spectra of the polymer-coated AuNPs were simulated based on the extinction cross sectional areas calculated from the Mie theory. 50 When the RI was fixed at 1.4, there was a slight increase and red shift from 531 to 538 nm in the LSPR band as the shell thickness increased from 0 to 20 nm (Fig. 3e). In contrast, the influence of RI on the LSPR band was much more prominent than thickness (Fig. 3f). As the RI increased from 1.4 to 1.7 and the thickness was fixed at 20 nm, the LSPR band significantly increased and red shifted from 531 to 566 nm, which is consistent with the polymerization processes observed in phenol and 2-CP (Fig. 2a&b). Our experimental data demonstrate that the light extinction of the polymers alone primarily occur in the UV region (Fig. S16). The weak light extinction they exhibit in the visible spectrum cannot lead to the observed shifts in the LSPR band (Fig. S16 and Fig. 3e&f), which we use to monitor polymerization kinetics (Fig. 4).

335

336

337

338

339

340

341

342

343

344

345

346

347

348

349

350

351

352

353

354

355

356

357

The thickness and density of the polymeric shells, which determine the LSPR band of polymer-coated AuNPs, are dependent on both the concentration and chemical structure of the polymer precursor. This is verified by both the TEM images and the extinction spectra. The polymer shells derived from 2,4-D were notably the thinnest and least dense, manifesting the smallest LSPR band shift (13 nm), which is attributed to the lowest concentration of 2,4-D (0.23).

mM, Fig. 3a). In comparison, the polymer shells derived from 2-CBA were visually thicker and denser, with a higher LSPR band shift (19 nm), due to its higher concentration (0.64 mM) than 2,4-D. Despite sharing the same concentration with 2-CBA, the polymer shells derived from 2-CP emerged as the thickest and most dense, aligning with its most pronounced red shift in the LSPR band (33 nm). In general, an elevated concentration and a favored chemical structure of the polymer precursor result in increased polymer thickness and density, which are reflected as an increase in LSPR band intensity and red shift.

CONCLUSIONS

Recent studies have proposed that instead of mineralizing all the organics in AOPs, the generation of polymers can be utilized as a novel strategy for organic removal. ^{10,33} With maximized polymer yield and appropriate separation, both carbon dioxide emission and oxidant dosage can be significantly reduced. ¹⁰ This dual benefit makes the polymerization strategy a promising and sustainable solution for the treatment of industrial wastewater that contains high levels of aromatic pollutants. Herein, our study presents an approach that enables the real-time and *in-situ* monitoring of polymerization kinetics for aromatic pollutants during persulfate-based AOPs. Through a comprehensive comparison of model compounds, we have gained insights into the influence of aromatic pollutant chemical structures, including funtional groups, chlorine substitution positions, and benzene ring quantities on their polymerization potential. Whether the AOPs are geared towards polymerization or mineralization, this rapid and cost-efficient approach can be employed to optimize the peroxide dosage and reaction time required for pilot-scale and full-scale deployment.

This method also enables a quantitative description of polymerization kinetics, thereby facilitating a deeper understanding of the polymerization mechanisms (Fig. 4). To normalize the

discrepancy between the LSPR band wavelength measured at each time point (WL_t) and the baseline wavelength at 0 min (WL₀), the values of WL_t-WL₀ were divided by the values of WL₀. Variations in the normalized LSPR wavelength shift (designated as "y") over 2 hours for all the phenolic compounds can be perfectly fitted into a pseudo-first-order kinetics model as depicted in Eq. S1 (see details in Text S7 and Fig. S17) and Fig. 4. Within this model, the parameter "b" represents the pseudo-first-order rate constant, while the parameter "a" signifies the intrinsic polymerization capacity of a chemical that can be determined by fitting the experimental data to Eq. S1. This intrinsic polymerization capacity is reflected as the density and thickness of the resulting polymers as elaborated earlier. The fitting results were summarized in Table S1.

As shown in Fig. 4a, phenol exhibited the fastest polymerization kinetics (b=0.097 min⁻¹) and highest polymerization capacity (a=0.062) among all the aromatic compounds possessing a single benzene ring. Equilibrium of the polymerization reaction was achieved after 45 min because of the depletion of phenol, rather than sulfate radicals. Our data indicate that the PDS concentration decreased by about 25% after a 120-min polymerization reaction (Fig. S17 and Text S7). This finding reinforces our initial hypothesis that sulfate radicals were present in excess relative to concentration of organic pollutants. While slower than phenol. the polymerization kinetics of 2-CP (b=0.043 min⁻¹) were considerably faster than 3-CP and 4-CP (0.031 and 0.029 min⁻¹), indicating that the introduction of a chlorine substituent to the meta and para positions of phenol leads to a more pronounced reduction in polymerization kinetics compared to a substitution at the ortho position. For 1-chloro-2-nitrobenzene and the two aliphatic carboxylates, the variations in their LSPR band wavelengths over 2 hours were minimal, rendering them inconsistent with the pseudo-first-order kinetics model (Fig. 4a).

Regarding the polymerization kinetics of aromatic carboxylates, e.g., 2-CBA and 2,4-D, a distinct "induction period" lasting for the initial 30 minutes was evident before the commencement of polymerization (Fig. S18). Unlike phenol and 2-CP, which exhibit enhanced reactivity towards SO₄*, both aromatic carboxylates had to compete with citrate (an aliphatic carboxylate employed in AuNP synthesis at a concentration of 0.2 mM) at the initial stage, thereby retarding their polymerization processes. At the same concentration (0.64 mM), the rate constant of 2-CBA polymerization (b=0.014 min⁻¹) was much lower than the phenolic compounds (Fig. 4a), highlighting the important role of functional groups in aromatic pollutant polymerization. Interestingly, 2-CBA at a lower concentration of 0.32 mM exhibited higher polymerization kinetics (b=0.025 min⁻¹), but a much lower polymerization capacity (a=0.040 for 0.64 mM vs. a=0.0066 for 0.32 mM). These results indicate that polymerization of aromatic carboxylates at low concentrations can rapidly reach the maximum point, which is simultaneously governed by the driving forces for polymerization and polymer degradation.

At a slightly lower concentration of 0.23 mM, 2,4-D demonstrated faster polymerization kinetics (b=0.030 min⁻¹) and a higher polymerization capacity (a=0.021) compared to 2-CBA (Fig. 4b), which is tentatively attributed to the higher complexicity of 2,4-D chemical structure. This hypothesis was subsequently validated by the much faster polymerization kinetics (b=0.15 min⁻¹) and higher polymerization potential (a=0.048) observed for DIC, a chemical with even higher structural complexicity. Co-existing ions in water matrices, such Cl⁻ and CO₃²⁻, can react with SO₄⁻ and potentially decelerate the polymerization reaction kinetics, especially at higher concentrations typically found in industrial wastewater. This impact will be quantitatively evaluated using this plasmonic colorimetric approach in our future studies. Overall, this *in-situ* and real time analytical method can be used to assess the polymerization kinetics and capacity for any

chemicals in a broad range of water matrices, offering an avenue to deepen our understanding of the mechanisms behind the formation of polymeric by-products during AOPs.

ASSOCIATED CONTENT

Supporting Information

428

429

430

431

432

433

434

435

436

437

438

439

440

441

442

443

444

445

446

447

Details of chemicals and equipments, AuNP synthesis, polymerization experimental settings, suspension purification, stability testing, TEM and EELS characterization, polymerization kinetics across varied PDS and 2-CBA centrations, and pseudo-first-order kinetics fitting (Text S1-7); TEM image of pristine AuNPs (Fig. S1); UV-vis spectrum of pristine AuNPs and spectral results of 2,4-D control experiments with PDS replaced by Milli Q water (Fig. S2); Kinetics of LSPR wavelength variations for different PDS and 2,4-D concentrations (Fig. S3); Spectral results of different PDS and 2,4-D concentration combinations (Fig. S4-6); Kinetics of LSPR wavelength variations for different PDS and 2-CBA concentrations (Fig. S7); Spectral results of different PDS and 2-CBA concentration combinations (Fig. S8-9); Spectral results of 2-CBA control experiments with PDS replaced by K₂SO₄ (Fig. S10); Spectral results of 3-CBA, 4-CBA, acetic acid, and chloroacetic acid (Fig. S11-12); Spectral results of dark control experiments for phenol, 2-CP, 3-CP, 4-CP, BPA, and DIC (Fig. S13); Spectral results of 1-chloro-2-nitrobenzene (Fig. S14); Spectral results of stability testing (Fig. S15); Spectral results of phenol under sunlit condition when AuNP was absent (Fig. S16); Raman spectral results of phenol experiments under sunlit condition (Fig. S17); Original variations in normalized LSPR wavelength shift for 2-CBA and 2,4-D in 2 hours (Fig. S18); Pseudo-first-order kinetics model fitting results (Table S1).

AUTHOR INFORMATION

Corresponding Author

148	Haoran Wei – Environmental Chemistry and Technology Program, Department of Civil
149	and Environmental Engineering, University of Wisconsin-Madison, 660 N Park St., Madison,
150	Wisconsin 53706.
151	Authors
152	Hanwei Wang – Environmental Chemistry and Technology Program, Department of Civil
153	and Environmental Engineering, University of Wisconsin-Madison, 660 N Park St., Madison,
154	Wisconsin 53706.
155	Alexander Kvit - Department of Materials Science and Engineering, University of
156	Wisconsin-Madison, 1509 University Avenue, Madison, Wisconsin 53706.
157	Author Contributions
158	This study was designed and manuscript was written by Hanwei Wang and Haoran Wei. TEM and
159	EELS characterization was conducted by Alexander Kvit.
160	Notes
161	The authors declare no competing financial interest.
162	ACKNOWLEDGEMENTS
163	The authors would like to thank the startup fund from the Department of Civil and Environmental
164	Engineering, College of Engineering, the Office of the Vice Chancellor for Research and Graduate
165	Education (OVCRGE) at the University of Wisconsin-Madison, and the Wisconsin Alumni
166	Research Foundation (WARF) for the support of this study. Additional support was provided by
167	the National Science Foundation (2132026).

469 REFERENCES

- 470 (1) Miklos, D. B.; Remy, C.; Jekel, M.; Linden, K. G.; Drewes, J. E.; Hubner, U. Evaluation of
- 471 Advanced Oxidation Processes for Water and Wastewater Treatment a Critical Review. Water
- 472 Res. **2018**, 139, 118-131.
- 473 (2) Yang, X.; Rosario-Ortiz, F. L.; Lei, Y.; Pan, Y. H.; Lei, X.; Westerho, P. Multiple Roles of
- Dissolved Organic Matter in Advanced Oxidation Processes. *Environ. Sci. Technol.* **2022**, *56* (16),
- 475 11111-11131.
- 476 (3) Von Gunten, U. Oxidation Processes in Water Treatment: Are We on Track? *Environ. Sci.*
- 477 *Technol.* **2018**, *52* (9), 5062-5075.
- 478 (4) Drossou, C.; Petrakis, Y.; Tyrovola, K.; Xekoukoulotakis, N. P. Photochemical Degradation
- of the Antidepressant Sertraline in Aqueous Solutions by UVC, UVC/H₂O₂, and UVC/S₂O₈².
- 480 Water Res. **2022**, 217.
- 481 (5) Anipsitakis, G. P.; Dionysiou, D. D. Degradation of Organic Contaminants in Water with
- Sulfate Radicals Generated by the Conjunction of Peroxymonosulfate with Cobalt. *Environ. Sci.*
- 483 *Technol.* **2003**, *37* (20), 4790-4797.
- 484 (6) Lee, J.; Von Gunten, U.; Kim, J. H. Persulfate-Based Advanced Oxidation: Critical Assessment
- of Opportunities and Roadblocks. *Environ. Sci. Technol.* **2020**, *54* (6), 3064-3081.
- 486 (7) Fang, J. Y.; Shang, C. Bromate Formation from Bromide Oxidation by the UV/Persulfate
- 487 Process. Environ. Sci. Technol. 2012, 46 (16), 8976-8983.
- 488 (8) Wei, H. R.; Loeb, S. K.; Halas, N. J.; Kim, J. H. Plasmon-Enabled Degradation of Organic
- 489 Micropollutants in Water by Visible-Light Illumination of Janus Gold Nanorods. *Proc. Natl. Acad.*
- 490 *Sci. U.S.A.* **2020**, *117* (27), 15473-15481.
- 491 (9) Lu, J. H.; Wu, J. W.; Ji, Y. F.; Kong, D. Y. Transformation of Bromide in Thermo Activated
- 492 Persulfate Oxidation Processes. *Water Res.* **2015**, 78, 1-8.

- 493 (10) Li, J. Y.; Liu, Z. Q.; Cui, Y. H.; Yang, S. Q.; Gu, J.; Ma, J. Abatement of Aromatic
- 494 Contaminants from Wastewater by a Heat/Persulfate Process Based on a Polymerization
- 495 Mechanism. Environ. Sci. Technol. 2023, 57 (47), 18575-18585.
- 496 (11) Li, Z. B.; Chen, Z.; Xiang, Y. Y.; Ling, L.; Fang, J. Y.; Shang, C.; Dionysiou, D. D. Bromate
- 497 Formation in Bromide-Containing Water through the Cobalt-Mediated Activation of
- 498 Peroxymonosulfate. *Water Res.* **2015**, *83*, 132-140.
- 499 (12) Anipsitakis, G. P.; Dionysiou, D. D.; Gonzalez, M. A. Cobalt-Mediated Activation of
- 500 Peroxymonosulfate and Sulfate Radical Attack on Phenolic Compounds. Implications of Chloride
- 501 Ions. Environ. Sci. Technol. **2006**, 40 (3), 1000-1007.
- 502 (13) Lu, J. H.; Dong, W.; Ji, Y. F.; Kong, D. Y.; Huang, Q. G. Natural Organic Matter Exposed to
- 503 Sulfate Radicals Increases Its Potential to Form Halogenated Disinfection Byproducts. *Environ*.
- 504 *Sci. Technol.* **2016**, *50* (10), 5060-5067.
- 505 (14) Sethna, S. M. The Elbs Persulfate Oxidation. *Chem. Rev.* **1951**, 49 (1), 91-101.
- 506 (15) Yang, S. Q.; Liu, Z. Q.; Cui, Y. H.; Wang, M. K. Organics Abatement and Recovery from
- Wastewater by a Polymerization-Based Electrochemically Assisted Persulfate Process: Promotion
- 508 Effect of Chloride Ion and Its Mechanism. J. Hazard. Mater. 2023, 446.
- 509 (16) Zhang, X. C.; Wu, S. H.; Jia, S. Y.; Wang, C.; Sun, S. W.; Wang, X. M.; Meng, Z. H.; Lin,
- 510 Y. Y.; Liu, Y.; Ren, H. T.; Han, X. Turning Thiophene Contaminant into Polymers from
- Wastewater by Persulfate and CuO. Chem. Eng. J. 2020, 397.
- 512 (17) Yang, Y.; Ren, W.; Hu, K.; Zhang, P.; Wang, Y.; Duan, X.; Sun, H.; Wang, S. Challenges in
- 513 Radical/Nonradical-Based Advanced Oxidation Processes for Carbon Recycling. Chem Catal.
- **2022**, 2 (8), 1858-1869.

- 515 (18) Liu, T. Y.; Wang, C.; Han, Y. Z.; Bai, C.; Ren, H. T.; Liu, Y.; Han, X. Oxidative
- Polymerization of Bisphenol A (BPA) Via H-Abstraction by Bi_{2.15}WO₆ and Persulfate: Importance
- of the Surface Complexes. Chem. Eng. J. 2022, 435.
- 518 (19) Anker, J. N.; Hall, W. P.; Lyandres, O.; Shah, N. C.; Zhao, J.; Van Duyne, R. P. Biosensing
- 519 with Plasmonic Nanosensors. *Nat. Mater.* **2008**, *7* (6), 442-453.
- 520 (20) Lee, K. S.; El-Sayed, M. A. Gold and Silver Nanoparticles in Sensing and Imaging: Sensitivity
- of Plasmon Response to Size, Shape, and Metal Composition. J. Phys. Chem. B 2006, 110 (39),
- 522 19220-19225.
- 523 (21) Xie, T.; Jing, C.; Long, Y. T. Single Plasmonic Nanoparticles as Ultrasensitive Sensors.
- 524 *Analyst* **2017**, *142* (3), 409-420.
- 525 (22) Willets, K. A.; Van Duyne, R. P. Localized Surface Plasmon Resonance Spectroscopy and
- 526 Sensing. Annu. Rev. Phys. Chem. **2007**, *58*, 267-297.
- 527 (23) Wei, H.; Abtahi, S. M. H.; Vikesland, P. J. Plasmonic Colorimetric and SERS Sensors for
- 528 Environmental Analysis. *Environ Sci-Nano* **2015**, *2* (2), 120-135.
- 529 (24) Reinhard, I.; Miller, K.; Diepenheim, G.; Cantrell, K.; Hall, W. P. Nanoparticle Design Rules
- for Colorimetric Plasmonic Sensors. ACS Appl. Nano Mater. 2020, 3 (5), 4342-4350.
- 531 (25) Wang, H.; Wei, H. Controlled Citrate Oxidation on Gold Nanoparticle Surfaces for Improved
- 532 Surface-Enhanced Raman Spectroscopic Analysis of Low-Affinity Organic Micropollutants.
- 533 *Langmuir* **2022**, *38* (16), 4958-4968.
- 534 (26) Wei, H. R.; Leng, W. N.; Song, J.; Willner, M. R.; Marr, L. C.; Zhou, W.; Vikesland, P. J.
- Improved Quantitative SERS Enabled by Surface Plasmon Enhanced Elastic Light Scattering.
- 536 Anal. Chem. **2018**, 90 (5), 3227-3237.

- 537 (27) Fontmorin, J.-M.; Fourcade, F.; Geneste, F.; Floner, D.; Huguet, S.; Amrane, A. Combined
- Process for 2,4-Dichlorophenoxyacetic Acid Treatment—Coupling of an Electrochemical System
- with a Biological Treatment. *Biochem. Eng. J.* **2013**, 70, 17-22.
- 540 (28) Kelly, K. L.; Coronado, E.; Zhao, L. L.; Schatz, G. C. The Optical Properties of Metal
- Nanoparticles: The Influence of Size, Shape, and Dielectric Environment. J. Phys. Chem. B 2003,
- 542 *107* (3), 668-677.
- 543 (29) Motamedi, M.; Yerushalmi, L.; Haghighat, F.; Chen, Z. Recent Developments in
- Photocatalysis of Industrial Effluents: a Review and Example of Phenolic Compounds
- 545 Degradation. *Chemosphere* **2022**, *296*, 133688.
- 546 (30) Dragstedt, C. A. The Halogenated Hydrocarbons: Their Toxicity and Potential Dangers. AMA
- 547 Arch. Intern. Med. 1956, 97 (2), 261-262.
- 548 (31) Davi, M. L.; Gnudi, F. Phenolic Compounds in Surface Water. Water Res. 1999, 33 (14),
- 549 3213-3219.
- 550 (32) Ahmad, M.; Teel, A. L.; Watts, R. J. Mechanism of Persulfate Activation by Phenols. *Environ*.
- 551 Sci. Technol. **2013**, 47 (11), 5864-5871.
- 552 (33) Wang, C.; Jia, S. Y.; Han, Y.; Li, Y.; Liu, Y.; Ren, H. T.; Wu, S. H.; Han, X. Selective
- Oxidation of Various Phenolic Contaminants by Activated Persulfate via the Hydrogen
- 554 Abstraction Pathway. ACS EST. Eng. **2021**, 1 (9), 1275-1286.
- 555 (34) Neta, P.; Madhavan, V.; Zemel, H.; Fessenden, R. W. Rate Constants and Mechanism of
- 856 Reaction of SO₄ with Aromatic Compounds. *J. Am. Chem. Soc.* **1977**, *99* (1), 163-164.
- 557 (35) Ji, Y. F.; Shi, Y. Y.; Yang, Y.; Yang, P. Z.; Wang, L.; Lu, J. H.; Li, J. H.; Zhou, L.; Ferronato,
- 558 C.; Chovelon, J. M. Rethinking Sulfate Radical-Based Oxidation of Nitrophenols: Formation of

- Toxic Polynitrophenols, Nitrated Biphenyls and Diphenyl Ethers. J. Hazard. Mater. 2019, 361,
- 560 152-161.
- 561 (36) Adeyi, A. A.; Babalola, B. A. Bisphenol-A (BPA) in Foods Commonly Consumed in
- Southwest Nigeria and Its Human Health Risk. Sci. Rep. 2019, 9.
- 563 (37) Shankar, A.; Teppala, S.; Sabanayagam, C. Bisphenol A and Peripheral Arterial Disease:
- Results from the Nhanes. *Environ. Health Perspect.* **2012**, *120* (9), 1297-1300.
- 565 (38) Meng, Z. Y.; Wang, D. Z.; Yan, S.; Li, R. S.; Yan, J.; Teng, M. M.; Zhou, Z. Q.; Zhu, W. T.
- Effects of Perinatal Exposure to BPA and Its Alternatives (BPS, BPF and BPAF) on Hepatic Lipid
- and Glucose Homeostasis in Female Mice Adolescent Offspring. Chemosphere 2018, 212, 297-
- 568 306.
- 569 (39) Oaks, J. L.; Gilbert, M.; Virani, M. Z.; Watson, R. T.; Meteyer, C. U.; Rideout, B. A.;
- 570 Shivaprasad, H. L.; Ahmed, S.; Chaudhry, M. J. I.; Arshad, M.; et al. Diclofenac Residues as the
- 571 Cause of Vulture Population Decline in Pakistan. *Nature* **2004**, *427* (6975), 630-633.
- 572 (40) Cunha, S. C.; Pena, A.; Fernandes, J. O. Mussels as Bioindicators of Diclofenac
- 573 Contamination in Coastal Environments. *Environ. Pollut.* **2017**, *225*, 354-360.
- 574 (41) Sathishkumar, P.; Mohan, K.; Meena, R. A. A.; Balasubramanian, M.; Chitra, L.; Ganesan,
- A. R.; Palvannan, T.; Brar, S. K.; Gu, F. L. Hazardous Impact of Diclofenac on Mammalian System:
- 576 Mitigation Strategy through Green Remediation Approach. J. Hazard. Mater. 2021, 419.
- 577 (42) Zhou, Q.; Luo, L.; Xia, L.; Cha, C.; Jiang, F.; Wang, H.; Dai, J.; Shu, L. Persulfate Enhanced
- Removal of Bisphenol A by Copper Oxide/Reduced Graphene Oxide Foam: Influencing Factors,
- 579 Mechanism and Degradation Pathway. *Chemosphere* **2023**, *340*, 139786.

- 580 (43) Cai, A.; Deng, J.; Ling, X.; Ye, C.; Sun, H.; Deng, Y.; Zhou, S.; Li, X. Degradation of
- Bisphenol A by UV/Persulfate Process in the Presence of Bromide: Role of Reactive Bromine.
- 582 Water Res. 2022, 215, 118288.
- 583 (44) Huang, Y.; Zou, J.; Lin, J.; Yang, H.; Wang, M.; Li, J.; Cao, W.; Yuan, B.; Ma, J. ABTS as
- Both Activator and Electron Shuttle to Activate Persulfate for Diclofenac Degradation: Formation
- and Contributions of ABTS⁺, SO₄⁻, and OH. *Environ. Sci. Technol.* **2023**, *57* (47), 18420-18432.
- 586 (45) Lu, X.; Shao, Y.; Gao, N.; Chen, J.; Zhang, Y.; Xiang, H.; Guo, Y. Degradation of Diclofenac
- by UV-Activated Persulfate Process: Kinetic Studies, Degradation Pathways and Toxicity
- 588 Assessments. *Ecotoxicol. Environ. Saf.* **2017**, *141*, 139-147.
- 589 (46) Donati, G.; Lingerfelt, D. B.; Aikens, C. M.; Li, X. Anisotropic Polarizability-Induced
- 590 Plasmon Transfer. J. Phys. Chem. C 2018, 122 (19), 10621-10626.
- 591 (47) Cheng, Y.; Smith, K. J.; Arinze, E. S.; Dziatko, R. A.; Gao, T.; Frank, B. P.; Thon, S. M.;
- 592 Bragg, A. E. Size- and Surface-Dependent Photoresponses of Solution-Processed Aluminum
- 593 Nanoparticles. *ACS Photonics* **2020**, *7* (3), 637-645.
- 594 (48) Lee, K. S.; El-Sayed, M. A. Gold and Silver Nanoparticles in Sensing and Imaging: Sensitivity
- of Plasmon Response to Size, Shape, and Metal Composition. J. Phys. Chem. B 2006, 110 (39),
- 596 19220-19225.

601

602

- 597 (49) Link, S.; El-Sayed, M. A. Optical Properties and Ultrafast Dynamics of Metallic Nanocrystals.
- 598 Annu. Rev. Phys. Chem. **2003**, *54*, 331-366.
- 599 (50) Oldenburg, S. J. Light Scattering from Gold Nanoshells. Dissertation, Rice University, 2000.

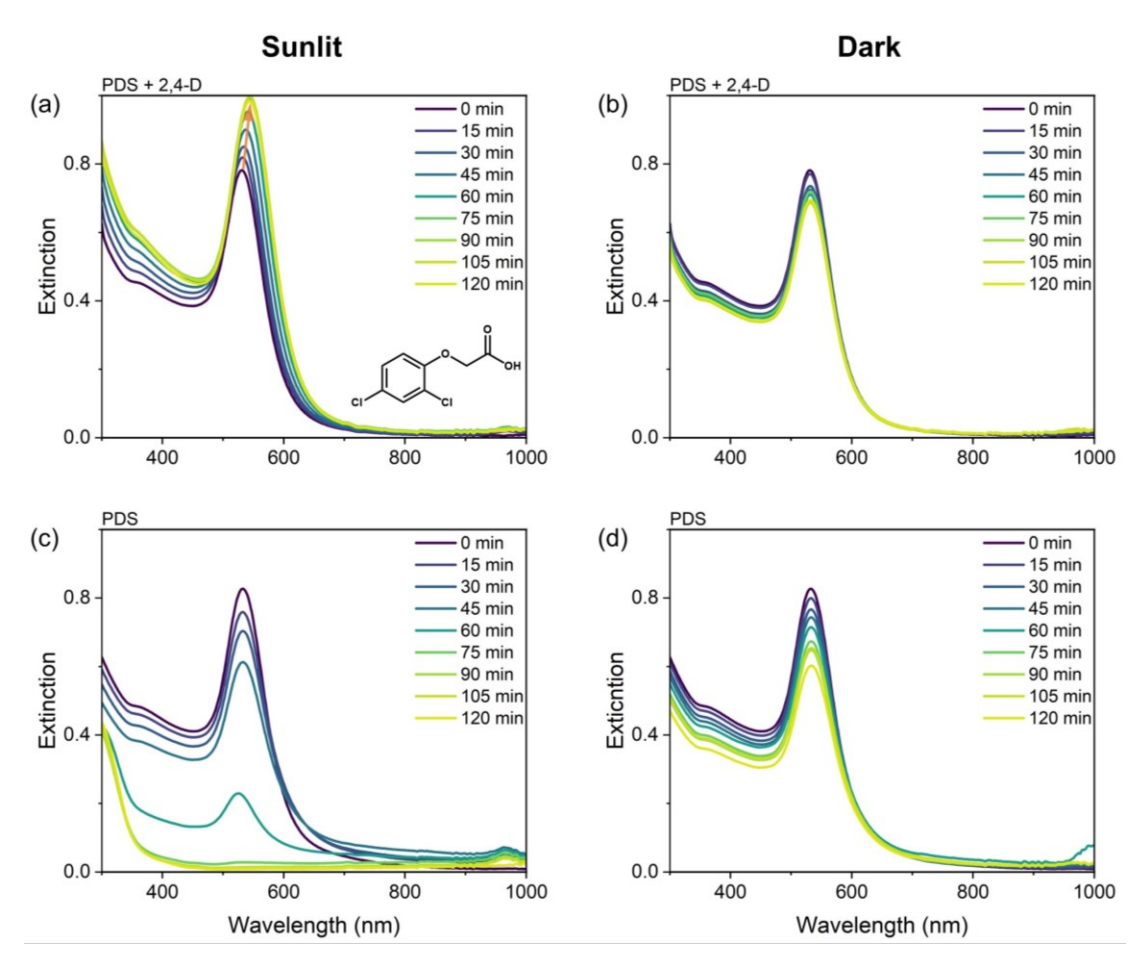


Figure 1. Variations in the UV-vis spectra of AuNP colloid with 5 mM PDS and 0.23 mM 2,4-D as a function of time under (a) sunlit and (b) dark conditions. Variations in the UV-vis spectra of AuNP colloid with 5 mM PDS as a function of time under (c) sunlit and (d) dark conditions. Simulated sunlight intensity: 2 Sun.

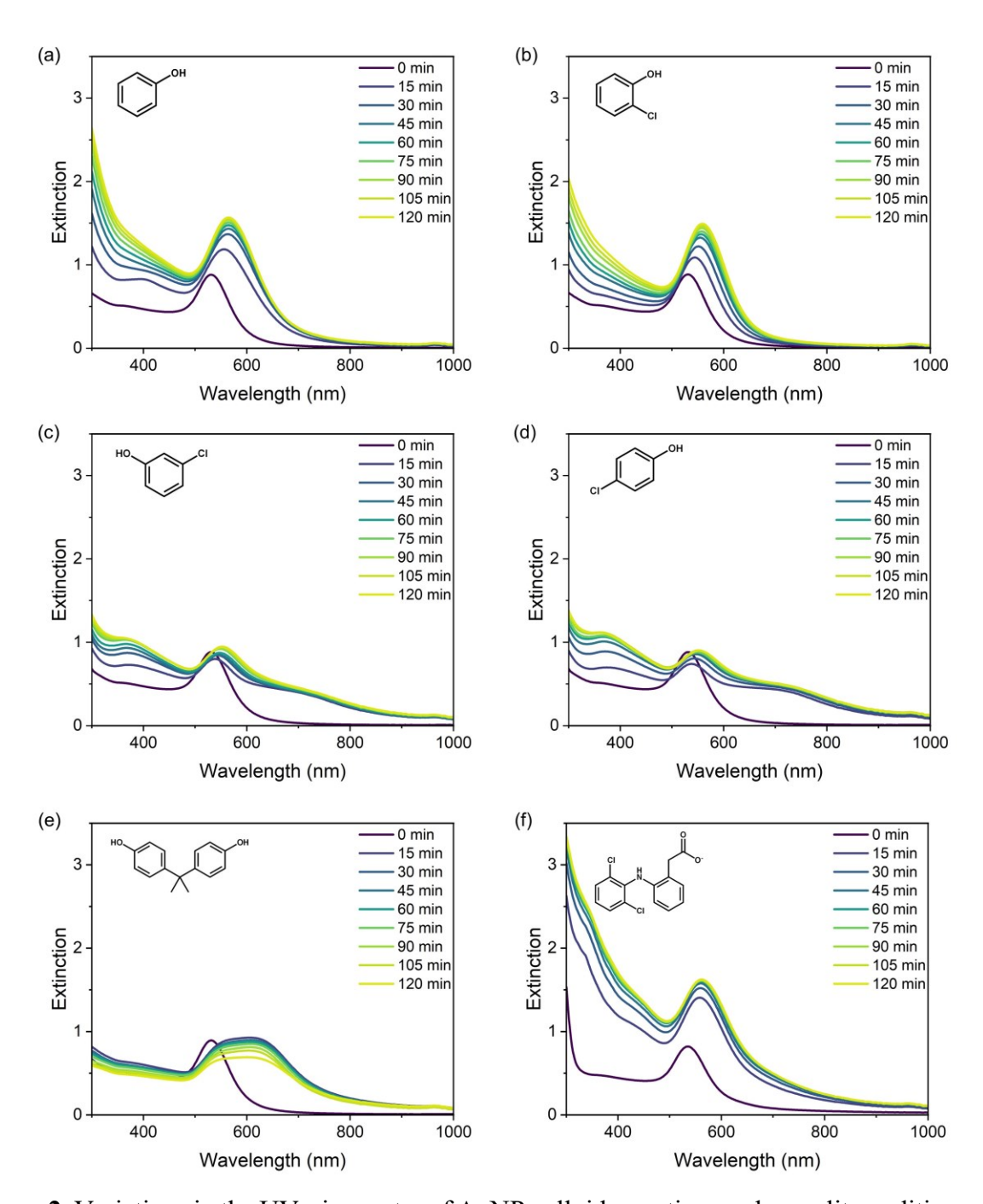


Figure 2. Variations in the UV-vis spectra of AuNP colloid over time under sunlit conditions, with 5 mM PDS and 0.64 mM (a) phenol, (b) 2-chlorophenol, (c) 3-chlorophenol, (d) 4-chlorophenol, (e) 0.055 mM BPA, and (f) 0.31 mM DIC. Simulated sunlight intensity: 2 Sun.

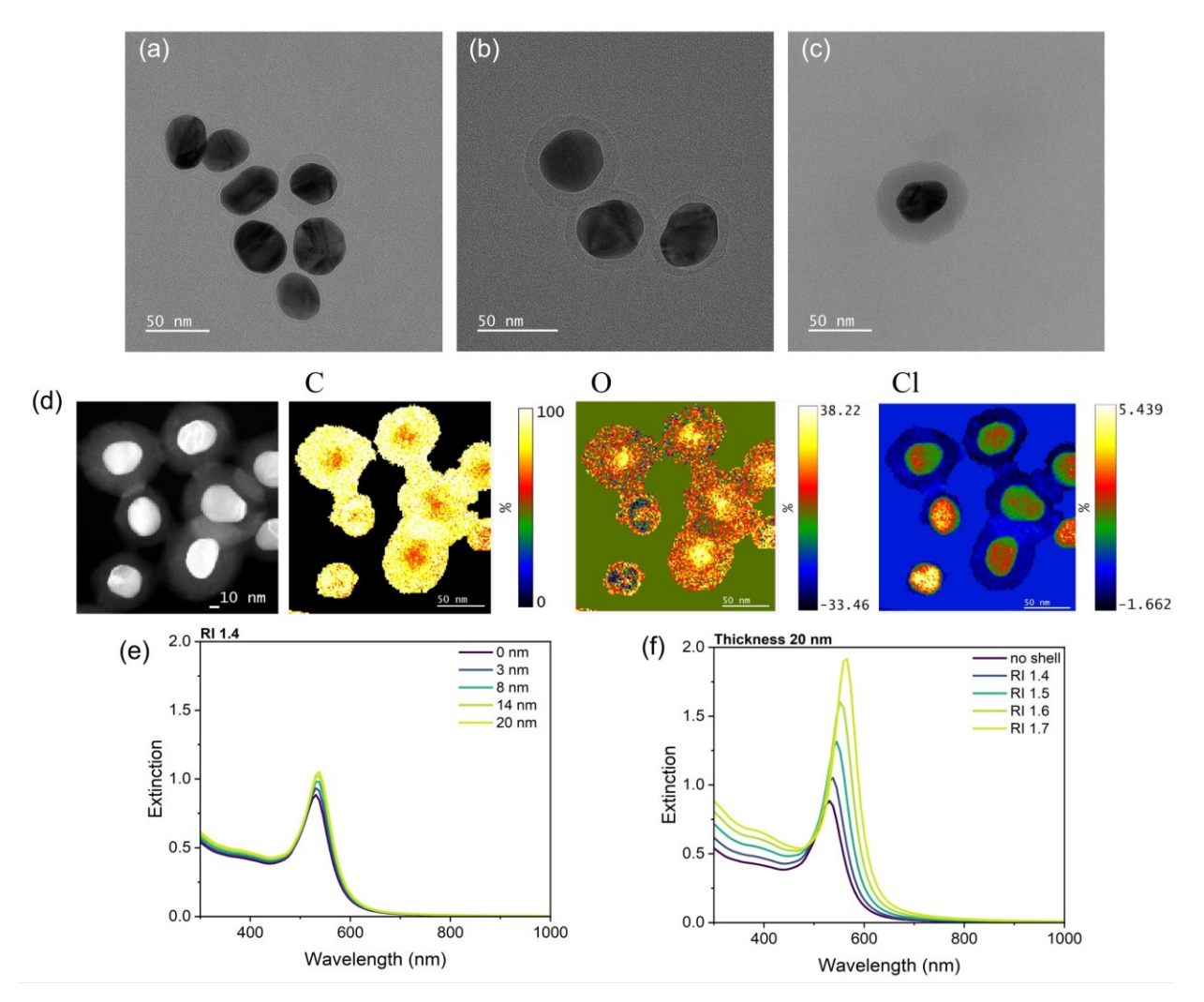


Figure 3. TEM images of polymer-coated AuNPs generated from the reactions of 5 mM PDS and (a) 0.23 mM 2,4-D, (b) 0.64 mM 2-CBA, and (c) 0.64 mM 2-CP under 2-hour simulated sunlight radiation. (d) HAADF-STEM image (left) and EELS spectrum images of the C, O, and Cl elements within the polymer-stabilized AuNPs generated from 2-CP. Simulated extinction spectra of polymer-coated AuNPs based on Mie theory when (e) the shell RI is fixed at 1.4 and (f) the shell thickness is fixed at 20 nm.

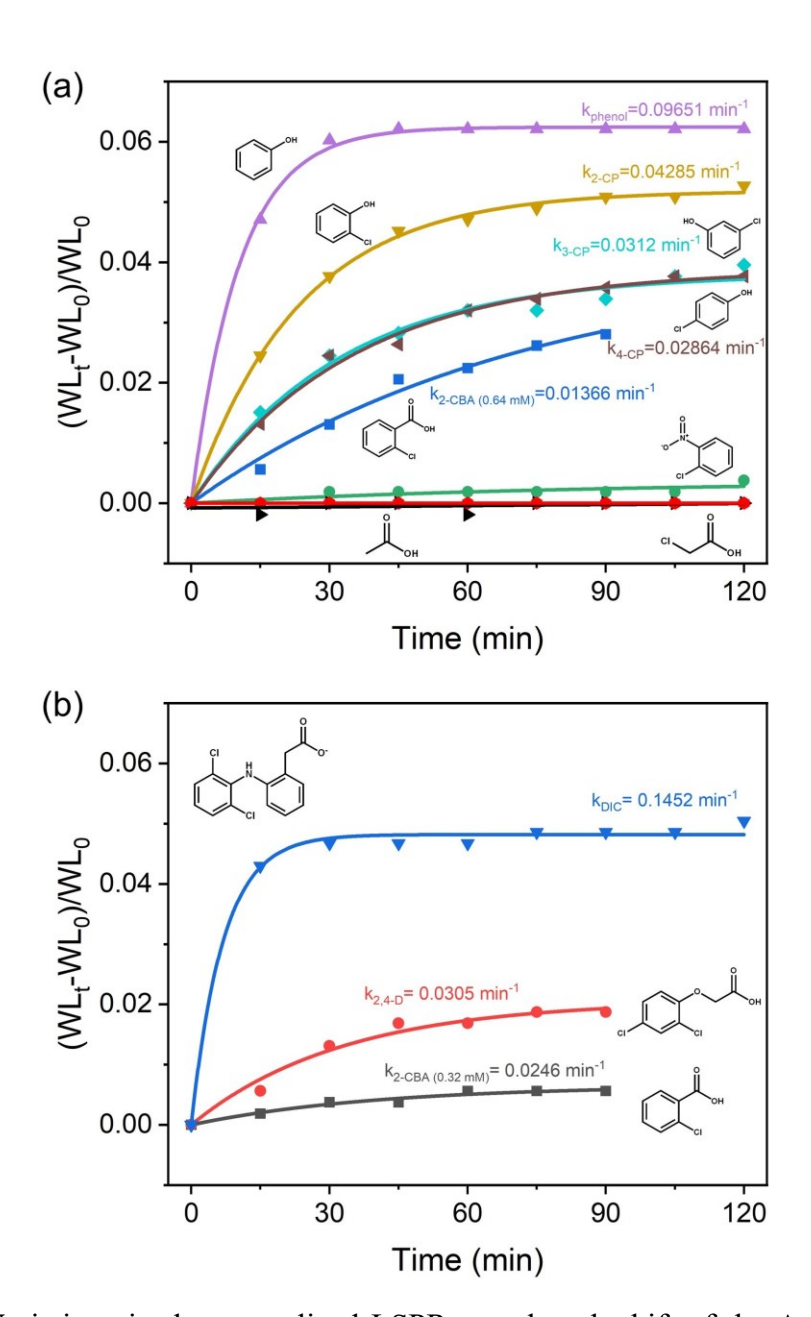


Figure 4. (a) Variations in the normalized LSPR wavelength shift of the AuNP colloid in the presence of 5 mM PDS and 0.64 mM phenol, 2-CP, 3-CP, 4-CP, 2-CBA, 1-chloro-2-nitrobenzene, acetic acid, and chloroacetic acid under sunlit conditions. Pseudo-first-order kinetics model regression was implemented for all the aroamatic compounds except 1-chloro-2-nitrobenzene. Linear regression was implemented for acetic acid, chloroacetic acid, and 1-chloro-2-nitrobenzene because of their minimal LSPR wavelength shifts. (b) Variations in the normalized LSPR wavelength shift of the AuNP colloid in the presence of 5 mM PDS and 0.32 mM 2-CBA, 0.23 mM 2,4-D, and 0.31 mM DIC under sunlit conditions. Pseudo-first-order kinetics model regression was implemented for all the three chemicals. Simulated sunlight intensity: 2 Sun.

634 TABLE OF CONTENTS ART

